Exploring the Effects of Intermetallic Particle Size and Spacing on the Corrosion of Mg-Al Alloys Using Model Electrodes

L. G. Bland,[a,*,z] N. Birbilis,[a,b,] and J. R. Scully[a,***]**

[a]*Department of Materials Science and Engineering, University of Virginia, Charlottesville, Virginia 22904, USA*
[b]*Department of Materials Science and Engineering, Monash University, Victoria 3800, Australia*

The effect of the area fraction, size and distribution of model cathodic, intermetallic particles (IMPs) in an anodic Mg matrix on corrosion was investigated. Model Mg-Al electrodes were developed to study IMP effects in isolation from other metallurgical effects, with particles simulated by Al electrodes embedded in a Mg matrix. Arrays of model Mg-Al electrodes were constructed using high purity Al as a surrogate for Al-rich IMPs and flush mounted in commercial purity Mg. The area fraction, size and spacing of these electrodes each altered the corrosion rate and cathodic reaction kinetics assessed after a 24 and 48 hour immersion period at the open circuit potential. Corrosion rate increased with increasing area fraction of Al electrodes but decreased with increasing electrode spacing given a fixed area fraction. The affected zone around electrodes and at the Al/Mg interface was explored to ascertain its impact on the resultant global corrosion rate and kinetics. The effect of local pH at the Al electrode on the prospects for Al corrosion and chemical redeposition were also explored.

Manuscript submitted August 22, 2016; revised manuscript received November 8, 2016. Published November 19, 2016.

Magnesium (Mg) alloys continue to be of growing interest due to their good balance of specific properties (i.e. properties relative to weight).[1–3] However, due to the inherently negative electrochemical potential of Mg and its alloys,[4,5] Mg-alloys are highly reactive compared to other engineering metals. Mg-alloys are susceptible to several forms of localized corrosion, whilst also highly prone to macro- as well as micro-galvanic corrosion. Due to the low solid solubility of most alloying elements in Mg[6] and particularly low solubility limits for most transition elements; secondary phases readily form during most types of material processing, including casting[7,8] and welding,[9–15] which can adversely alter the corrosion performance.

There are many secondary phases, or intermetallic particles (IMPs), which are particularly common in Mg alloys. Each IMP[16] has its own unique dissolution or reduction kinetics, dependent on its composition, size and dispersion within the material. For example, in the Mg-Al alloys which contain Mn (such as AZ31, AZ91 and AM50), Al-Mn IMPs that are rich in Al such as Al_4Mn, Al_6Mn, display relatively low rates of cathodic kinetics in comparison to other IMPs that are rich in Mn such as Al_8Mn_5; the latter displaying relatively rapid cathodic kinetics.[1,7,17] Similarly, the so called Al-Mn-Fe IMPs, such as $Al_8(Mn,Fe)_5$ function as highly potent cathodic sites in Mg, although the Mn has been shown to prevent some of the detrimental galvanic effects of Fe impurities by incorporating the Fe into the Al-Mn IMPs.[1,6,16] Furthermore, Mg-Zn IMPs have approximately the same open circuit potential (OCP) as many Mg alloys. However, the cathodic kinetics of this IMP are more rapid than Mg,[16] attributed to the presence of Zn. Mg-Zn IMPs are cathodic to the α-Mg and, therefore, tend to cause localized corrosion through micro-galvanic coupling which is often manifest at the Mg matrix/IMP interface. Some of these trends are outlined in Table I. However, the effects of so-called 'cathodic' IMPs with regard to the dissolution they cause upon the α-Mg matrix require further attention, particularly regarding of how the size and location/spacing of IMPs alter the overall corrosion rate.

Of relevance to the corrosion of Mg and its alloys, it has been suggested[18–21] that the exchange current density for the hydrogen evolution reaction (HER) increases with the rate of Mg dissolution. Meanwhile, other workers have used spatial and temporal methods to determine that Mg dissolution is accompanied by enhanced cathodic activity on the Mg surface.[19,22–26] Cathodically active sites have been examined through the use of scanning vibrating electrode technique (SVET) on 99.9%[25] and 99.99%[23] pure Mg, Mg-Nd binary alloys[24] and AZ31.[22,27] To date, mechanisms have been proposed, which explain this behavior, including: (i) transition metal enrichment from impurities,[28,29] (ii) particle enrichment to the oxide layer[26,30,31] and (iii) Al redeposition.[30]

Evidence of cathodic activation has been noted to also be influenced by cathodic sites upon the Mg sample surface, namely intermetallic particles (IMPs) and impurities.[19,26,32] However, it has also been demonstrated that most of the hydrogen evolution reaction (HER) on corroding Mg-alloys occurs at the anodic front (i.e. the sites of active dissolution).[21] The dissolution of Mg at these sites has been observed to develop as dark regions which propagate through the a mechanism with filiform-like morphology typically cited on many Mg alloys, including AZ31 and AM30.[32,33] The Mg-alloy corrosion rate was also found to correlate with the percent area of these dark, corroded regions in chloride environments.[9,34] Rapid HER on Mg-alloys was also correlated with increased corrosion or cathodic activity at these dark sites.[20,21] Furthermore, this enhanced cathodic activity on the surface can occur due to Al alkaline corrosion and subsequent chemical redeposition as well as transition metal enrichment from impurities.[28,29] Al can be dissolved due to cathodic or alkaline dissolution of Al-rich IMPs due to a local pH increase during galvanically induced corrosion, enabling the $Al \rightarrow AlO_2^-$ and/or $Al \rightarrow Al_2O_3$

Table I. Open circuit potential for various Al containing IMPs.[1,16,42,43]

IMP	Solution	Open Circuit Potential (V_{SCE})
Commercial purity Mg	0.1 M NaCl	−1.55
Commercial purity Mg	0.6 M NaCl	−1.65
Commercial purity Mg	5 M NaCl	−1.67
Al_6Mn	0.85 M NaCl + $Mg(OH)_2$	−1.52
Al_4Mn	0.85 M NaCl + $Mg(OH)_2$	−1.45
Al_8Mn_5	0.85 M NaCl + $Mg(OH)_2$	−1.25
$Mg_{17}Al_{12}$	0.85 M NaCl + $Mg(OH)_2$	−1.2
$Mg_{17}Al_{12}$	0.1 M NaCl	−1.2
Al_8Mn_5Fe	0.85 M NaCl + $Mg(OH)_2$	−1.2
Al_4Mn	0.85 M NaCl + $Mg(OH)_2$	−1.15
$Al_6Mn(Fe)$	0.85 M NaCl + $Mg(OH)_2$	−1.1
High purity Al	0.6 M NaCl	−1.0
$Al_6(MnFe)$	0.85 M NaCl + $Mg(OH)_2$	−1.0
$Al_3Fe(Mn)$	0.85 M NaCl + $Mg(OH)_2$	−0.95
Al_3Fe	0.85 M NaCl + $Mg(OH)_2$	−0.74
Mg_2Al_3	0.85 M NaCl + $Mg(OH)_2$	−1.18

*Electrochemical Society Student Member.
**Electrochemical Society Member.
***Electrochemical Society Fellow.
[z]E-mail: bland.117@osu.edu

reaction when thermodynamically possible at IMPs.[30,35,36] As these Al-rich particles corrode, they can be enriched within the metal oxide layer.[26,30,32,37] Such selective dissolution of Al would constitute dealloying, and during this dealloying process, the Al-Mn particle (Al_8Mn_5 in most cases) is able to transform to Mn-O oxide (such as Mn_3O_4).[30] This transformation or dealloying process has been noted and empirically shown elsewhere.[30,38] Following selective dissolution, Al can then redeposit upon the Mg-alloy surface. The redeposited alloying elements can enhance the rates of HER.[30]

The objective of the present work was to analyze how the size, area fraction and distribution of Al-rich IMPs impact the corrosion rate of Mg-Al alloys. In a related study exploiting the heat-treatment of AZ31B (3 wt% Al, 2 wt% Zn, 1 wt% Mn, bal. Mg) to vary particle size and spacing, it was found that small reactive particles were more detrimental to the corrosion rate than larger particles.[39] In this study, the Al-Mn particles were 0.1–0.8 μm in diameter and spaced 10–30 μm while the Al-Mn-Fe particles were 5–10 μm and spaced at greater distances (50 μm–100 μm) from center-to-center, depending on heat-treatment.[39] However, heat-treatment could change other factors such as grain size, IMP composition and even the α-Mg matrix composition. It was noted that the area and volume fraction of these IMPs remained approximately the same for each heat-treatment time and temperature.[39] To better understand the effect of IMP size and distribution, without influence from other metallurgical characteristics, model Mg-Al arrays were utilized. These model samples were developed considering these particles as arrays of high cathodic, Al electrodes embedded in the anodic Mg matrix. The model alloys were constructed using high purity Al electrodes as a surrogate for Al-rich IMPs. It is also important to emphasize that the model alloys herein are simplified so that the spacing and area fraction of Al can be altered, without the simultaneous alteration of matrix Al-content or the IMPs. This is an important distinction, as the present study aims to focus upon the corrosion kinetic factors as a function of cathode size and geometry. This is different to studying the role of Al-content, which has been summarized recently elsewhere.[40]

Experimental

Materials.—Extruded commercially pure Mg rod (99.9%) was supplied by Alfa Aesar as well as 99.999% Al and 99.99% Fe electrodes (varying in diameter from 1 mm to 0.25 mm). Only the Al electrode arrays were analyzed within the full analysis, however a brief comparison of the corrosion morphology due to electrode composition is discussed. The composition of the commercially pure Mg is reported in wt%, as provided by QUANT (Quality Analysis and Testing Corporation) (0.01% Al, 0.01% Mn, 0.01% Zn, 0.021% Si, 0.005% Cu, 0.001% Ni, 0.006% Fe and Mg Bal). The bare electrodes were prepared by successive grinding with silicon-carbide paper and rinsing with ethanol to a final grit of 1200 prior to testing. Compositional analysis did not detect any Al redistribution during sample preparation (before electrochemical testing).

Model samples for intermetallic particle size and distribution.—Model Mg-Al arrays were developed with flush mounted pure Al electrodes embedded in commercial purity Mg (Figure 1) with variations in the area fraction of Al electrodes as well as variations in the electrode size and spacing to test these characteristics in isolation, without concern of influence from outside metallurgical characteristics (i.e. grain size, IMP phase transformations, material residual stresses) which may affect the intrinsic corrosion rate. Al wires of various diameters were embedded in holes on the Mg surface that were approximately the same size as the Al wires. No crevice corrosion was observed at the Mg/Al interface.

A typical range of dissolution of reduction kinetics for various Al-containing IMPs seen in Mg alloys.[16] High purity Al has been chosen as a surrogate because it has a measured OCP (−0.9 V_{SCE}) within the range of electrochemical potentials for some of the Al-containing IMPs in Mg, in comparison to the commercial purity Mg matrix (−1.65 V_{SCE}) as detailed in Table I. For the purposes of this analysis, it is assumed that the pure Al electrode will behave similar to Al_xMn_y IMPs.[16,41,42]

To test differences in the corrosion kinetics with area fraction, 1 mm diameter Al electrodes were embedded in the Mg with different area fractions of high purity Al, brought about by increasing the number of Al electrodes (of equivalent diameter) in the Mg. The corrosion kinetics of the entire array were compared to the as-received Mg corrosion rate, as previously reported for 0.6 M NaCl at OCP.[43] The variation in the electrode area fraction, diameter and spacing are reported in Table II. The variation in the corrosion kinetics with electrode size were tested using Al electrodes with varying diameters (1 mm, 0.5 mm and 0.25 mm) while retaining the same area fraction of Al (Table II). This required using a different number of electrodes, embedded in the Mg, depending on the electrode diameter. The spacing of these electrodes was varied from 3 mm to 7 mm to test how the electrode spacing altered the corrosion kinetics. The Al electrodes were shorted to the Mg such that the sample was one planar electrode.

Model samples were analyzed with scanning electron microscopy (SEM) using a FEI Quanta 650 microscope to determine the composition of any Al-containing oxides at the electrode edge. Compositional analysis was performed using energy dispersive spectroscopy (EDS) methods[44] on the as-corroded specimens with full consideration of the ZAF corrections (Z is the atomic number correction, A is the absorption correction and F is the fluorescence correction) on the Aztec software tool.[44] Images were recorded at a working distance of 10 mm while operating at an accelerating voltage of 5 kV. The extent of corrosion damage was determined using the ImageJ software package.[45] 3D images were also obtained using a Hirox optical microscope to determine the depth of corrosion where the ASTM G1-03 standard chromic acid solution (200 g/L CrO_3) was used to remove any corrosion product.[46] The 3D profile of the corrosion damage was profiled using the *MountainMaps* software package.[47]

Corrosion rate determination.—Array electrodes were exposed at OCP in 0.6 M NaCl in ambient conditions for 24 hours with intermittent electrochemical impedance spectroscopy (EIS) measurements taken at frequencies from 10 kHz–10 mHz. The pH of this solution was initially ∼5.3 and was measured to be ∼11 after 24 hours. EIS scans were analyzed and fit using the software program ZView to an equivalent circuit, seen in Figure 2. The relative corrosion rate was determined using the polarization resistance, R_p, where the corrosion rate, $i_{corr} \propto 1/R_p$:[43,48]

$$\frac{1}{R_p} = \frac{1}{R_1 + R_2} + \frac{1}{R_3} \quad [1]$$

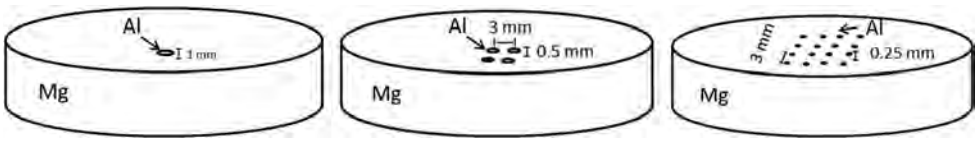

Figure 1. Model sample designs indicate varying the Al-electrode diameter while retaining the same total Al area fraction. Samples were also created with variations in the area fraction by adding more electrodes at the same diameter and spacing. The electrode spacing was varied from 3 to 7 mm. Al used was 99.999% pure metal basis, whilst Mg matrix was commercially pure.

Table II. Design of model Mg-Al alloys with variations in the area fraction of Al electrodes embedded in Mg. Variations in the electrode size and spacing. Aluminum is 99.999% pure metal.

Number of electrodes	Al Electrode Diameter (mm)	Al Electrode Spacing (mm)	Area of Mg (mm^2)	Area of Al (mm^2)	Al Area Fraction	
–	–	–	791.7	–	–	–
1	1[a]	–	790.9	0.785	0.001	Vary Al Area
2	1[a]	5	790.1	1.590	0.002	
3	1[a]	5	789.3	2.390	0.003	
4	1[a]	5	788.5	3.190	0.004	
4	0.5[b,c]	3	790.9	0.785	0.001	Vary Spacing
4	0.5[c]	4	790.9	0.785	0.001	
4	0.5[c]	5	790.9	0.785	0.001	
4	0.5[c]	6	790.9	0.785	0.001	
4	0.5[b,c]	7	790.9	0.785	0.001	
16	0.25[b,c]	3	790.9	0.785	0.001	Vary Spacing
16	0.25[c]	4	790.9	0.785	0.001	
16	0.25[c]	5	790.9	0.785	0.001	
16	0.25[c]	6	790.9	0.785	0.001	
16	0.25[b,c]	7	790.9	0.785	0.001	

[a]Discussed in Figures 5–7.
[b]Discussed in Figures 8–10.
[c]Discussed in Figures 11–13.

R_1, R_2, and R_3 are the respective resistance values where R_1 and R_2 are in series and both are in parallel with R_3. The experimental setup consisted of a three-electrode electrochemical flat cell with a 1 cm^2 sample window. For simplification, only EIS determined R_p was determined as it has been shown previously to yield similar corrosion rates as determined from hydrogen evolution, inductively coupled optical emission spectroscopy solution analysis and gravimetric mass loss.[9,43,48] A Pt mesh was used as a counter electrode and a saturated calomel electrode (SCE) was used as the reference electrode. The Bode magnitude and phase plots are typical fits, determined through at least three replicates.

Cathodic kinetics were determined in unbuffered 0.6 M NaCl and buffered tris(hydroxymethyl)aminomethane (TRIS) for 3, 24 and 48 hours at OCP, which is followed by a cathodic potentiodynamic polarization scan ranging from 0.5 V above OCP to −2.3 V_{SCE} below OCP in a downward sweep at a rate of 1 mV/second. At least three cathodic polarization curve replicates were run with the average cathodic current density, i_c, (as determined at −1.8 V_{SCE}) reported.

The galvanic current between Mg and Al were determined using a zero resistance ammeter (ZRA) in a flat cell.[49,50] The samples were coupled with the Mg as the working electrode (WE) and Al as the counter electrode (CE). The cathode to anode ratio was varied from 2:1, 1:1 and 1:2. The Mg anode size remained the same while the Al cathode was increased to examine how the cathode area affected the corrosion current density. The effect of the anodic polarization induced by galvanic coupling of the Mg in close contact with Al-rich phases was determined through potentiostatic polarization at the Mg-Al galvanic couple potential (−1.63 V_{SCE}) for 24 hours in 0.6 M NaCl.

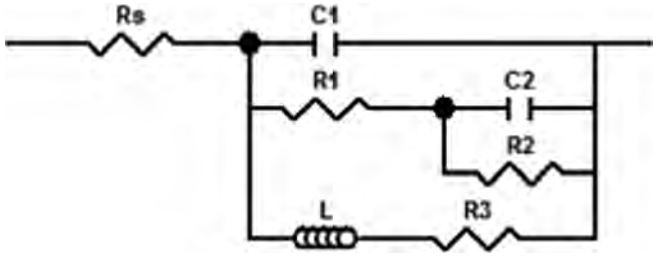

Figure 2. Equivalent circuit used to model pseudo-inductive electrochemical impedance response on corroding Mg in 0.6 M NaCl.

Variation in the pH of the solution was examined using a universal pH solution on a Mg-Al array embedded with one 1 mm Al electrode. A thin layer of the 0.6 M NaCl solution (initial pH ∼5.3) and 0.1 M TRIS (pH ∼7) was deposited on top of the sample and left for approximately 10 minutes. Local pH was established quickly. An approximate value for the local pH levels on the surface was determined from a universal pH standard.

Results

Imaging of the effect of intermetallic particle material on galvanic corrosion.—Samples with the same area fraction of electrodes (each spaced 5 mm from center-to-center) were immersed at OCP in 0.6 M NaCl for 3 hours to examine the corrosion morphology. Samples with the same area fraction and electrodes measuring 0.25 mm and 0.5 mm showed slightly more localized corrosion at the electrode and somewhat non-uniform corrosion across the electrode surface (Figures 3a–3b). However, samples with one 1 mm electrode had more localized corrosion at the Al-Mg interface with less corrosion farther away from the electrode (Figure 3c). Concerning Fe model electrodes in comparison to Al, the Mg area around the Al electrode affected by corrosion was approximately 750 μm while the corrosion area around the Fe electrode was approximately 1500 μm (Figures 3c–3d). The depth of the corrosion attack was similar at 600 μm ± 300 μm in most cases. It was observed, on the 1 mm diameter wires (Figures 3c–3d) there was a "zone of exclusion" where there was little to no corrosion attack. This is most likely due to the variation in the pH gradient away from the Al and/or Fe electrode. The effect of pH on corrosion will be discussed.

As the area of the Al increased, in an Al:Mg galvanic couple, the galvanic couple current density and galvanic couple potential increased (Figures 4a–4b). Typical potentiostatic data of Mg over a 24 hour period, taken by applying the galvanic couple potential (−1.43 V_{SCE}) indicated a net anodic charge with time (Figure 4c). The net anodic current decreased around approximately 100 to 1000 seconds during polarization to −1.43 V_{SCE} which implies an inhibition in the anodic dissolution reaction rate or an increase in the cathodic reaction rate. This is trend correlates with a net anodic current decrease found at similar anodic potentials on commercial purity Mg undergoing anodically induced cathodic activation.[28]

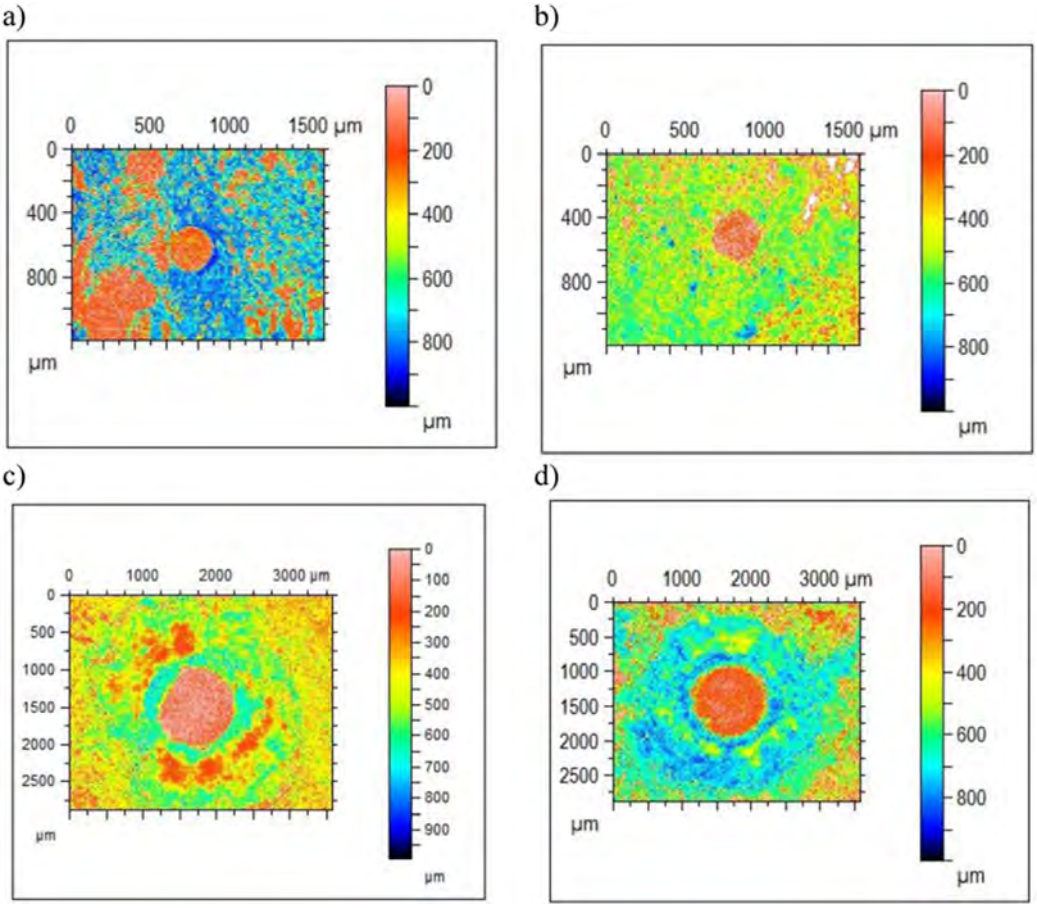

Figure 3. Variation in the 3D corrosion morphology for Mg electrode arrays with various electrode diameters and array electrode materials. Samples were immersed in 0.6 M NaCl for 3 hrs at OCP and cleaned with chromic acid (CrO_3) to remove any oxide product. a) 0.25 mm Al electrode, b) 0.5 mm Al electrode, c) 1 mm Al electrode and d) 1 mm Fe electrode. All samples retained the same area fraction of electrodes, although only one electrode is shown.

EIS of Mg-Al electrode arrays.— *Effect of electrode area fraction for a fixed diameter and spacing on the corrosion rate.*—Figure 5a contains the Bode magnitude and phase plots for the commercial purity Mg, embedded with increasing area fractions of high purity Al electrodes, as described in Table II for samples in 0.6 M NaCl. The Al electrodes in each case had a diameter of 1 mm and were spaced 5 mm apart from center-to-center. The capacitive elements were adequately represented by conventional capacitors, as opposed to constant phase elements, and experimental EIS data had a good fit where the error% (of the fit, as designated as the ZView output) was estimated at less than 20% for each run. The as-received commercial purity Mg had the highest measured frequency dependent impedance and lowest $1/R_p$.[43] The relative corrosion rate was determined for each area fraction over the full 24 hour immersion as $1/R_p$ (Figure 5b) where $1/R_p$ increased with the area fraction of Al.

It is similarly shown that the cathodic kinetics of the system increase with Al area fraction (Figures 6a–6b) in 0.6 M NaCl. However, even though $1/R_p$ increased by a factor of 4 (Figure 6b), the increase in the cathodic kinetics, assessed at -1.8 V_{SCE}, was by several orders of magnitude. The cathodic kinetics for samples immersed in 0.1 M TRIS displayed very little variation with increasing Al area fraction, with only a slight increase brought about by the addition of Al to the electrode (Figure 7b). This is characteristic of this electrolyte, which displays little to no cathodic activation.[10]

Effect of electrode diameter on the corrosion rate.—The effect of electrode diameter and spacing, with constant Al area fraction, on $1/R_p$ is shown in Figure 8 for 0.6 M NaCl for two electrode spacings and three electrode diameters. The spacing of the electrodes was varied between 3 mm to 7 mm while the wire diameters were 0.25 mm, 0.5 mm and 1 mm. The number of wires embedded in the Mg was varied to yield a constant area fraction (Table I). The Mg-Al array with 16 Al electrodes, each with a 0.25 mm diameter, had the lowest measured R_p and therefore the highest relative corrosion rate ($1/R_p$). The Mg-Al array with 1 Al electrode, measuring 1 mm in diameter, had the lowest overall $1/R_p$ (Figure 8). The cathodic kinetics, as determined at -1.8 V_{SCE}, increased with decreasing Al electrode size (Figure 9) in 0.6 M NaCl, given the same variations in Al. However, the cathodic kinetics in 0.1 M TRIS were approximately the same for all Al–containing samples (at constant Al area fraction) and greater than that of Mg (Figure 10). In summary, closely spaced, small electrodes had the highest reaction rate in chloride-containing environments, given the same area fraction of Al (as larger electrodes), but little variation was detected in the non-chloride containing environment.

Effect of electrode spacing on the corrosion rate.—The variation in the electrode spacing, with constant Al diameter and area fraction, on corrosion rate and cathodic kinetics are shown in Figures 11 and 12 for 0.6 M NaCl. Plotted as a function of $1/R_p$ (Figure 11), the relative corrosion rate increased with decreasing electrode spacing for a fixed Al electrode diameter and area fraction. A typical set of cathodic polarization curves for Mg electrodes embedded with 0.5 mm electrodes with different electrode spacings are shown in Figure 12a in 0.6 M NaCl. The cathodic kinetics in 0.6 M NaCl, as determined at -1.8 V_{SCE} (Figures 12b–12c) revealed that, as the electrode spacing increased (for a fixed Al electrode area fraction), the rate of the HER decreased for both 0.5 mm and 0.25 mm electrodes. A typical set of cathodic polarization curves for Mg electrodes embedded with 0.5 mm electrodes with different electrode spacings are shown in Figure 13a in 0.1 M TRIS. The cathodic kinetics in 0.1 M TRIS, as determined

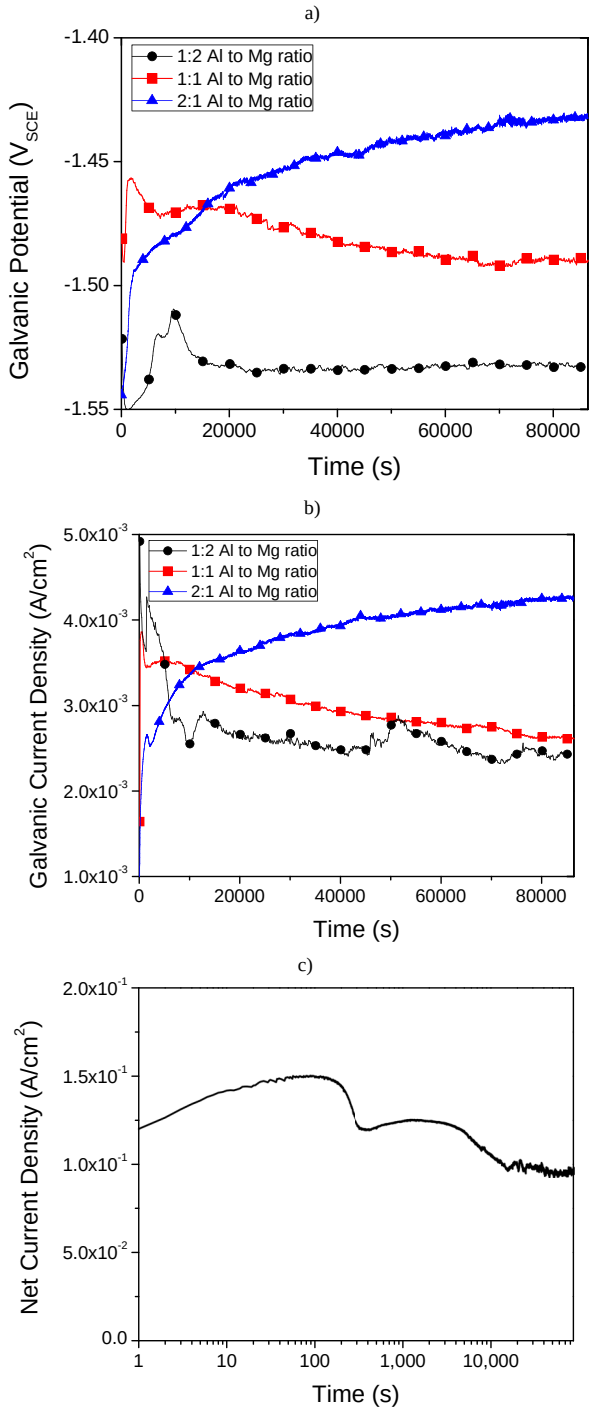

Figure 4. a) Galvanic potential and b) galvanic current density of Mg-Al couple in 0.6 M NaCl with a 2:1, 1:1 and 2:1 Cathode:Anode ratio. c) potentiostatic polarization of 99.9% commercial purity Mg over 24 hrs in 0.6 M NaCl taken at the galvanic couple potential of Mg to Al (−1.43 V_{SCE}).

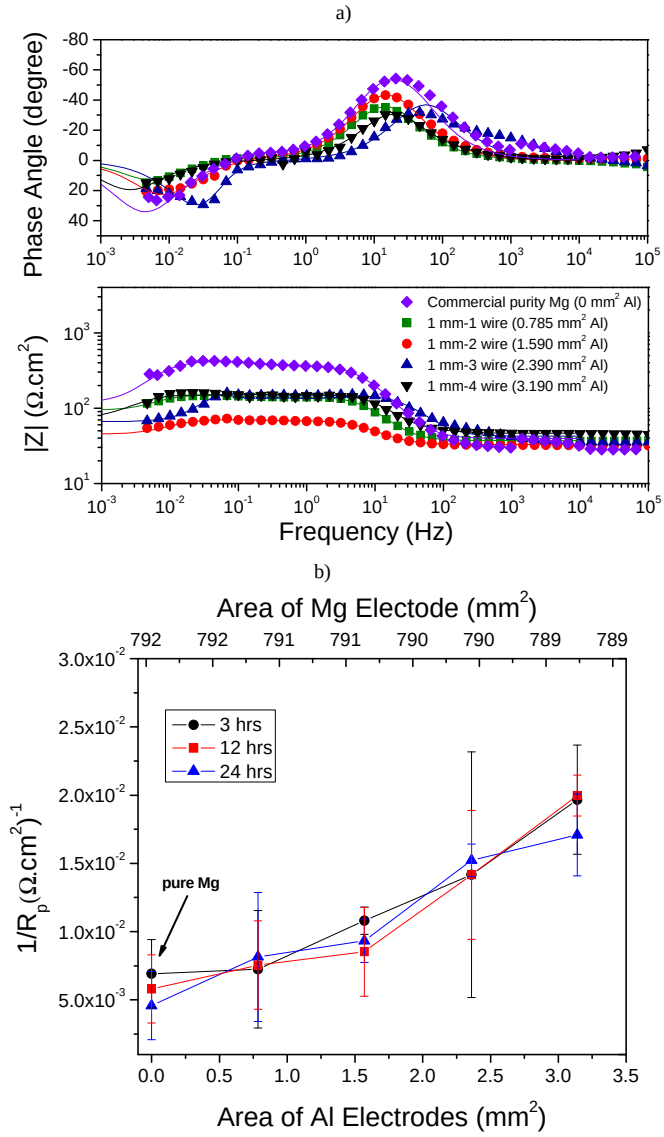

Figure 5. a) Bode phase and magnitude plot and b) EIS determined polarization resistance for commercial purity Mg embedded with increasing area fraction of 1 mm diameter high purity Al electrodes, each spaced 5 mm apart. Data shown along with respective fits was taken following 24 hour immersion in 0.6 M NaCl at OCP.

at −1.8 V_{SCE} (Figures 13b–13c) were approximately the same for all electrode spacings but was consistently greater than that observed for Mg without Al electrodes.

Variation in pH with surface location.—The variation pH with surface location was determined in a thin film environment for both 0.6 M NaCl and 0.1 M TRIS (Figures 14a–14c). A key for the pH measurement, as determined by a universal pH indicator, is contained in Figure 14a. The region directly above and adjacent to the Al electrode became highly alkaline (pH ∼11), according to the universal pH indicator, in the 0.6 M NaCl (Figure 14b). Spreading of high pH away from the Al electrode was observed immediately after the universal pH solution was added (Figure 14c). However, in the buffered, 0.1 M TRIS environment, there was much less variation in the pH, indicating that the TRIS buffer retains a pH of ∼7–8, even in the rapidly dissolving Mg-Al environment (Figure 14d). From SEM and EDS analysis of the Al electrode and the corroded interface in 0.6 M NaCl, the largest amount of dissolution occurred at this interface (Figure 15a). The oxide formed during dissolution contains Al (Figure 15b).

Discussion

Effects of a potential distribution field at the electrode interface on the corrosion rate.—The resultant, accelerated corrosion due to an array of cathodic phases embedded in Mg was assessed. The extent of corrosion attack was dependent on the electrode material embedded in α-Mg matrix, where Fe was much more active than Al (Figure 3).[16] The relative global corrosion rate, assessed by $1/R_p$, along with the corresponding cathodic kinetics, were evaluated (Figures 5–13). When

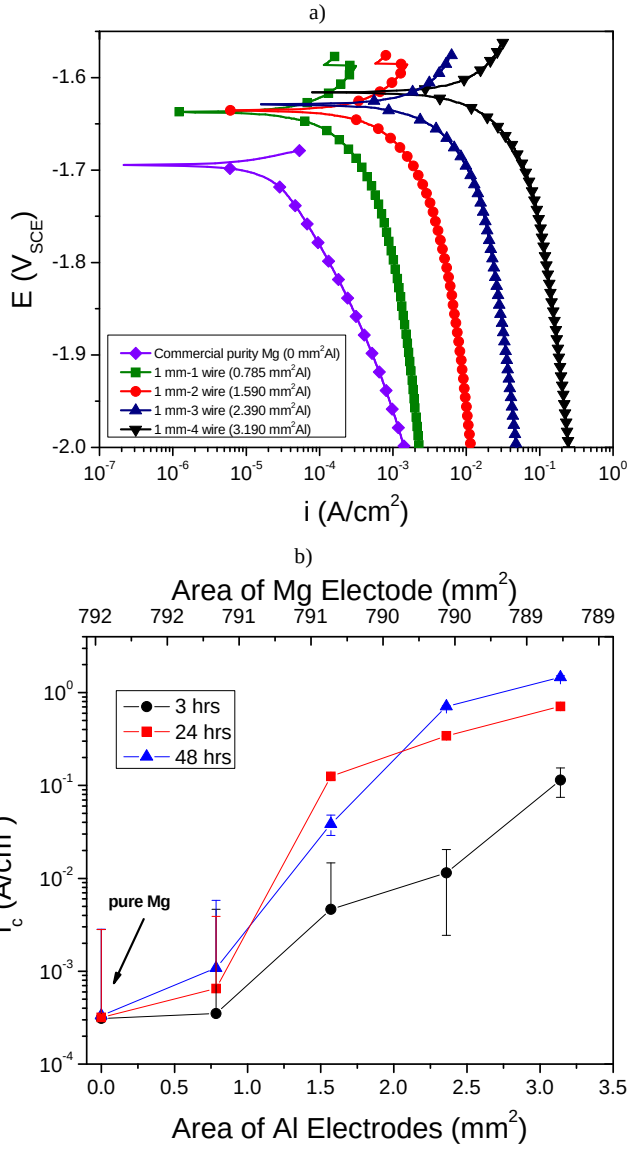

Figure 6. a) typical cathodic polarization curves and b) variation in cathodic kinetics of the HER represented by i_c as a function of the area of high purity Al electrodes embedded in Mg with increasing area of 1 mm diameter high purity Al electrode(s), each spaced 5 mm apart. Al electrodes with different area fraction from 1 Al electrode to 4 Al electrodes embedded in Mg. Cathodic kinetics were determined from cathodic polarization at −1.8 V_{SCE} after 3, 24 and 48 hour holds at OCP in 0.6 M NaCl solution.

Al was embedded in Mg, the potential was likely elevated in a zone around the Al electrode. This potential elevation, due to each electrode in the array, will increase the corrosion rate of Mg in its vicinity. The variation in the extent of corrosion can be understood by considering the potential distribution around a single cathodic electrode using an analytical solution of the Laplace equation.[51,52] Consider the case where the radius of an electrode or cluster of electrodes is d, the polarization resistance of the alloy is R_p (as determined from EIS measurements[43]), E_c is the OCP for the electrode, E_m is the OCP of the matrix, ρ is the solution resistivity, d is the electrode diameter and r is the radial distance from the edge of the electrode. In this case, the elevated potential distribution with radial distance (E(r)) can be described using Equation 2.[53]

$$E(r) = E_c - (E_m - E_c)\exp\left[-\left(\frac{3\rho}{4R_p d}\right)^{\frac{1}{2}} r\right] \qquad [2]$$

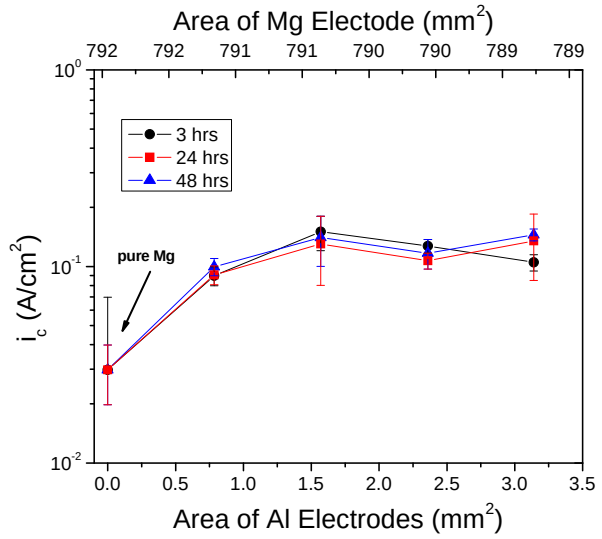

Figure 7. Variation in cathodic kinetics as a function of the area of high purity Al electrodes for commercial purity Mg embedded with increasing area of 1 mm high purity Al electrodes, each spaced 5 mm apart. Al electrodes with different area fraction from 1 Al electrode to 4 Al electrodes embedded in Mg. Cathodic kinetics determined from cathodic polarization curves taken at −1.8 V_{SCE} after 3, 24 and 48 hour holds at OCP in 0.1 M TRIS solution.

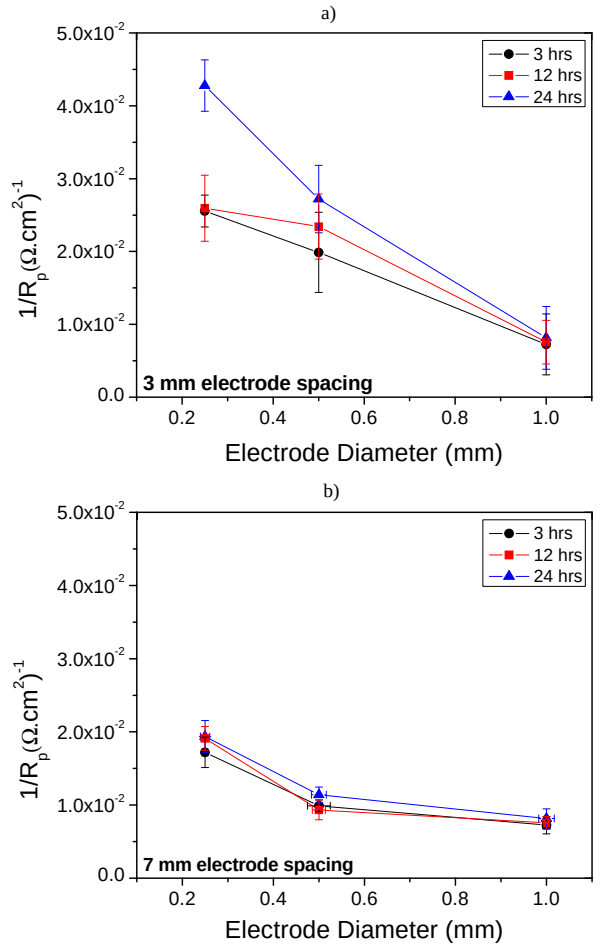

Figure 8. Variation in the polarization resistance as a function of the electrode diameter over 24 hours at OCP. Commercial purity Mg embedded with high purity Al electrodes of different diameters from 1 mm to 0.25 mm. The area fraction of high purity Al electrodes was kept constant at 0.001 by retaining an area of 790.9 mm² of commercial purity Mg and 0.785 mm² of high purity Al. The spacing of these electrodes was a) 3 mm and b) 7 mm.

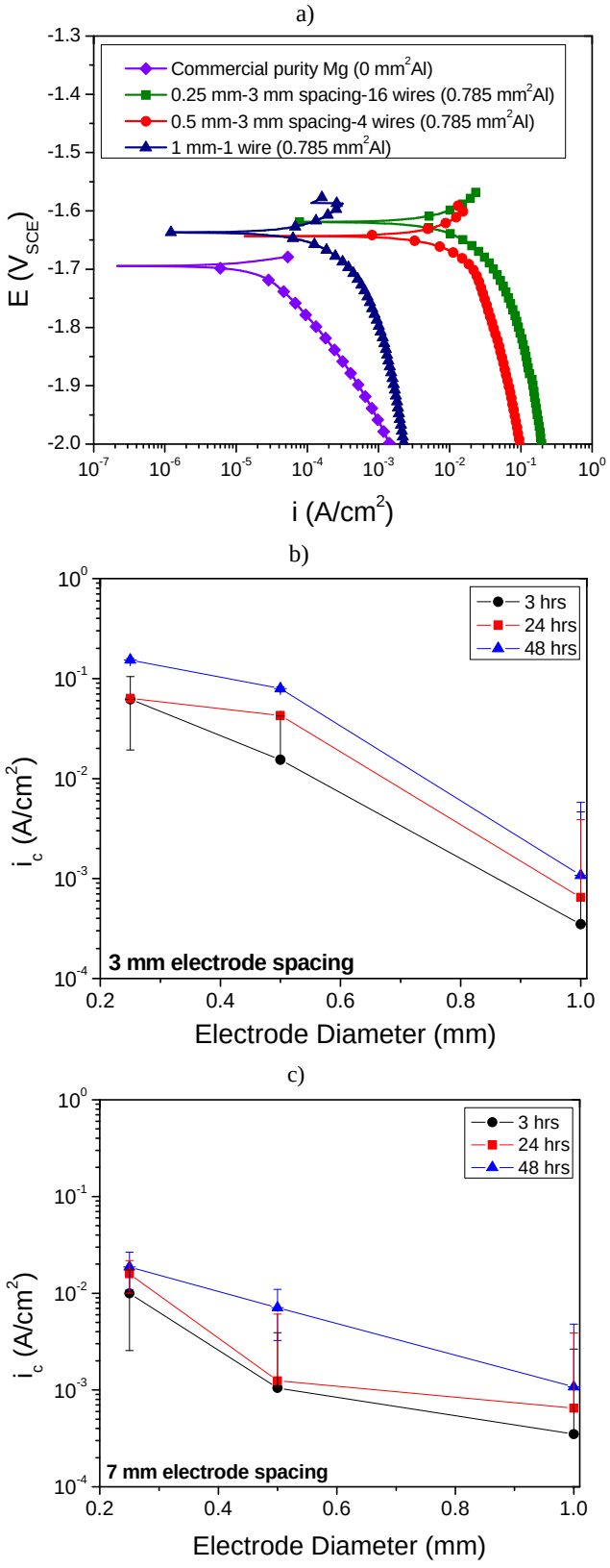

Figure 9. Variation in cathodic kinetics with Al electrode diameter. Commercial purity Mg embedded with high purity Al electrodes of different diameters from 1 mm to 0.25 mm. The area fraction of high purity Al electrodes was kept constant at 0.001 by retaining an area of 790.9 mm^2 of commercial purity Mg and 0.785 mm^2 of high purity Al. Typical cathodic polarization curves for a) 3 mm. Cathodic current densities determined from cathodic polarization curves taken at −1.8 V_{SCE} after 3, 24 and 48 hour holds at OCP in 0.6 M NaCl for b) 3 mm and c) 7mm diameter electrodes.

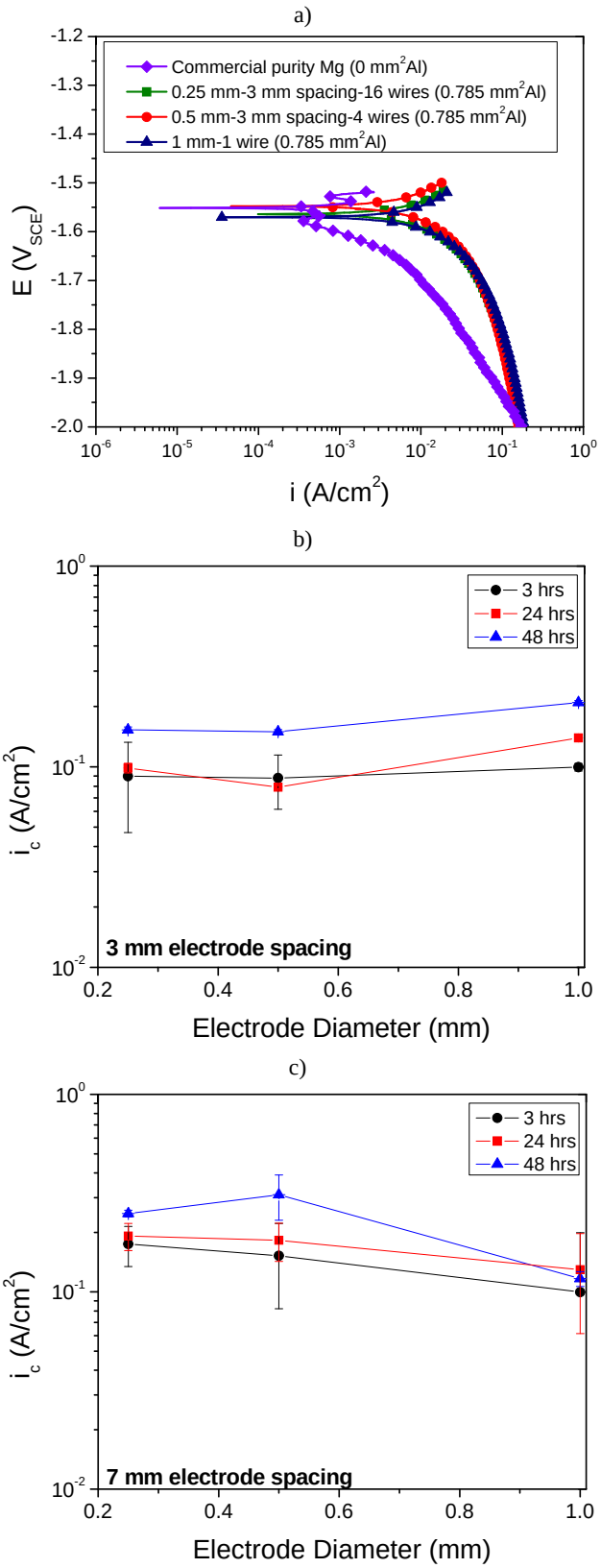

Figure 10. Variation in cathodic kinetics with the Al electrode diameter. Commercial purity Mg embedded with high purity Al electrodes of different diameters from 1 mm to 0.25 mm. The area fraction of high purity Al electrodes was kept constant at 0.001 by retaining an area of 790.9 mm^2 of commercial purity Mg and 0.785 mm^2 of high purity Al. Typical cathodic polarization curves for a) 3 mm. Cathodic current density determined from cathodic polarization curves taken at −1.8 V_{SCE} after 3, 24 and 48 hour holds at OCP in 0.1 M TRIS for b) 3 mm and c) 7mm diameter electrodes.

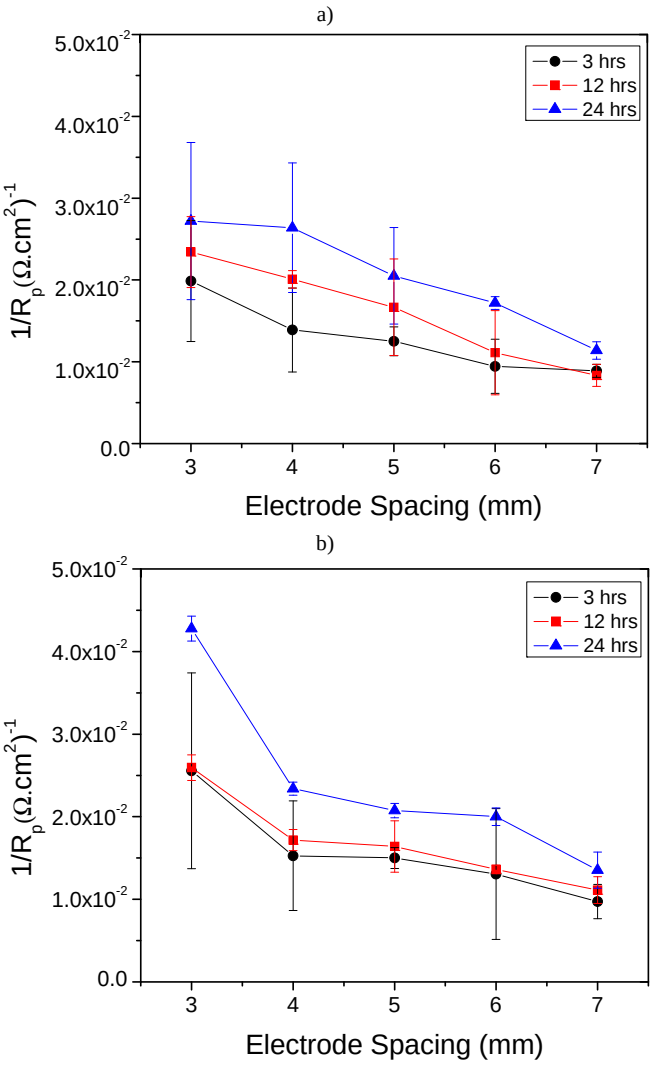

Figure 11. Variation in polarization resistance with electrode spacing for a) 0.50 mm diameter and b) 0.25 mm diameter high purity Al electrodes embedded in commercial purity Mg. The area fraction of high purity Al electrodes was kept constant at 0.001 by retaining an area of 790.9 mm^2 of commercial purity Mg and 0.785 mm^2 of high purity Al.

The E(r) estimated via Equation 2 is plotted in Figure 16 for both an Al and a Fe electrode. It is clear that E(r) is elevated for a radial distance of ~2000/4000 μm. The potential distribution around the electrode, E(r), may trigger (anodic dissolution induced) cathodic activation of the nearby Mg-matrix in this zone, as is seen in many Mg-alloys[26,32,33] - with corrosion initiation and propagation proximate to cathodic electrodes. For electrodes with different compositions but the same area fraction and electrode size, as presented for both Al and Fe electrodes in Mg (Figure 3), it was observed that the affected radial zone around the Fe electrode was larger than that around the Al electrode because the Fe electrode is a 'stronger cathode', whereby it has more rapid HER kinetics for a given cathodic potential. Equation 2, also showed that E(r) around a Fe electrode was larger than around an Al electrode - with E(r) increasing with increasing electrode diameter for both electrode compositions (Figures 16a–16b).

However, when the number of electrodes was varied but the area fraction and composition of these electrodes remained constant, the analysis can become more complicated as a multitude of electrodes must be accounted for. Under the premise that the amount of anodically induced cathodic activation (occurring due to Al redistribution of transition metal enrichment at the particle interface[28,29]) can be determined through considering the sum of all anodically induced zones

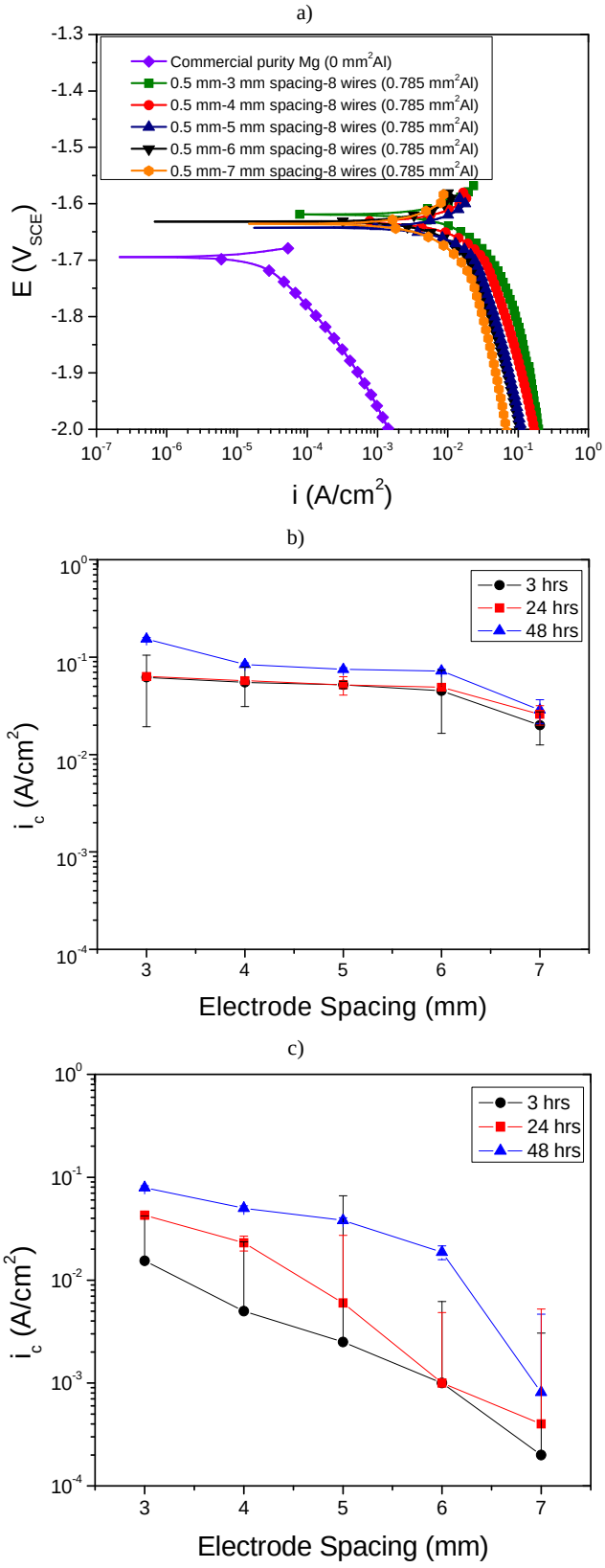

Figure 12. Variation in cathodic kinetics with the Al electrode spacing. Commercial purity Mg embedded with high purity Al electrodes of different diameters from 1 mm to 0.25 mm. The area fraction of high purity Al electrodes was kept constant at 0.001 by retaining an area of 790.9 mm^2 of commercial purity Mg and 0.785 mm^2 of high purity Al. Typical cathodic polarization curves for a) 3 mm. Cathodic current density was determined from cathodic polarization curves taken at −1.8 V_{SCE} after 3, 24 and 48 hour holds at OCP in 0.6 M NaCl for b) 3 mm and c) 7mm diameter electrodes.

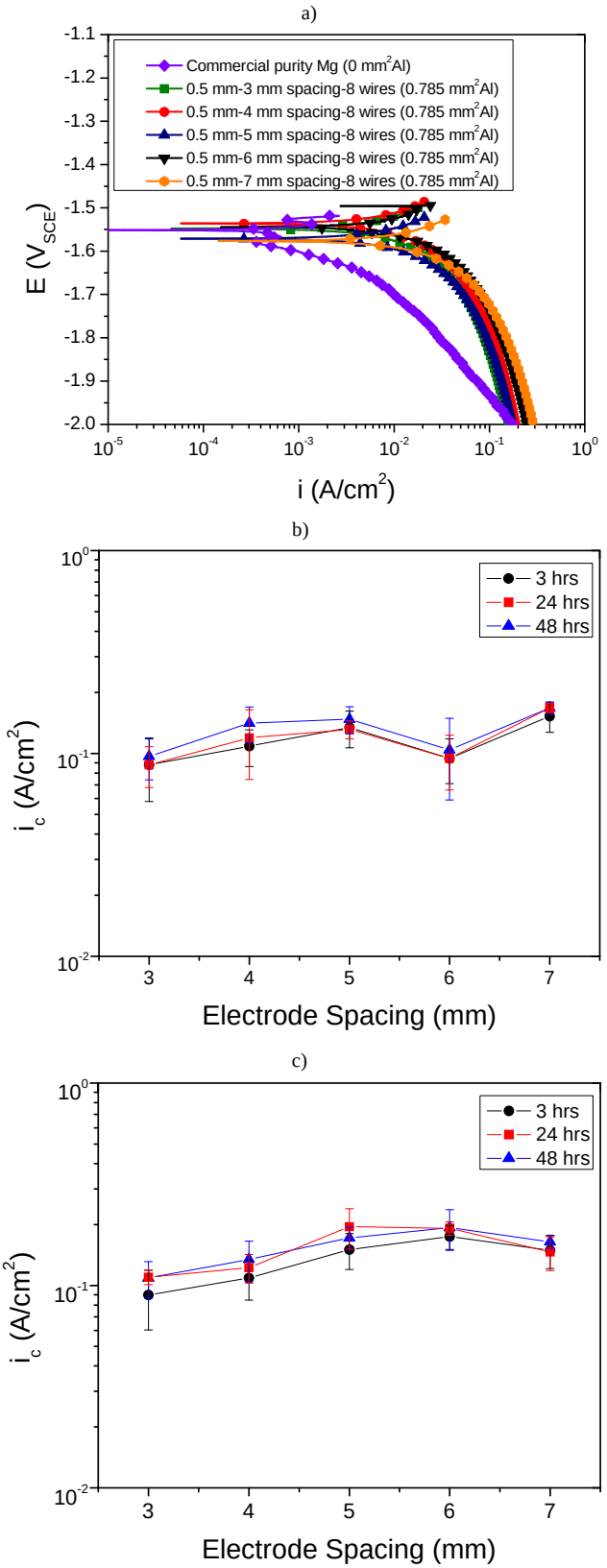

Figure 13. Variation in cathodic kinetics with Al electrode spacing. Commercial purity Mg embedded with high purity Al electrodes of different diameters from 1 mm to 0.25 mm. The area fraction of high purity Al electrodes was kept constant at 0.001 by retaining an area of 790.9 mm^2 of commercial purity Mg and 0.785 mm^2 of high purity Al. Typical cathodic polarization curves for a) 3 mm. Cathodic current density was determined from cathodic polarization curves taken at −1.8 V_{SCE} after 3, 24 and 48 hour holds at OCP in 0.1 M TRIS for b) 3 mm and c) 7mm diameter electrodes.

(A^{AIZ}) around the electrode by relating it to the number of electrodes, N, the extent of anodically induced cathodic activation across an entire sample surface with multiple electrodes can be approximated by:

$$A^{AIZ} = \pi(r_{zone})^2\,(N) \qquad [3]$$

Where N is the number of electrodes or, in the case of the Mg-Al arrays, the number of Al electrodes embedded in Mg and r_{zone}∼E(r) where potential is elevated. With the same area fraction (but different numbers of electrodes, N), there is a decrease in the E(r) via Equation 2 on the sample surface for a given electrode size, as determined for 0.25 mm, 0.5 mm and 1 mm diameter electrodes (Figure 17). However, N is much greater such that the smaller value of r_{zone} is more than compensated for by the increase in N when there are many small electrodes. This means that the overall A^{AIZ} on the sample is much higher for those samples with more electrodes containing on the sample surface. From the 3D corrosion morphology of at the Mg/Al electrode interface (Figure 3), a localized corrosion morphology was seen for the 1 mm electrode case, while a non-localized, more spread out corrosion morphology was seen for the 0.25 and 0.5 mm electrode cases due to the presence of multiple electrodes (to retain the same area fraction). This reflects A^{AIZ} increasing for small electrodes (Figure 17).

The effect of the electrode area fraction on the EIS determined corrosion rate and the cathodic kinetics determined from polarization testing was also observed in 0.6 M NaCl (Figures 5–6). As the area fraction of electrodes increased, the corrosion rate similarly increased in 0.6 M NaCl As more cathodic Al electrodes were embedded into the Mg, there were more cathodically activated regions (leading to a larger overall A^{AIZ}), as seen in Figure 17. As the area of the Al increased and the area of the Mg decreased which led to more galvanic attack since the Al electrodes function as active sites for the HER. This trend has been previously noted for Mg-Fe galvanic couples where the corrosion rate dramatically increases with an increasing Fe:Mg ratio.[54] The galvanic couple current density and potential are seen to increase with cathode:anode ratio (Figures 4a–4b). The galvanic potential between Mg and Al is more positive in comparison to the OCP of Mg, therefore polarizing the Mg sample anodically. Such a scenario is similar to the case when the Mg sample is held at −1.43 V_{SCE} for 24 hrs (Figure 4c). Enhanced catalytic activity on the sample surface would be expected. This is particularly important because, while the A^{AIZ} area is about ten times larger, the increase in the cathodic kinetics is on the order of 1000 times larger. Therefore, the effect of the Al redistribution, as well as the enhanced cathodic activity (due to metal enrichment from impurities[28,29]), both increased the overall cathodic reaction rate dramatically as seen in Figure 7b.

As the electrode size increases, with the same area fraction, there are fewer electrodes for cathodic activation (Figures 8–10). But the radius of the potential distribution around the electrode E(r) extends to larger r (Figure 16). However, E(r) fields do not overlap as the spacing between electrodes becomes larger than r_{zone}. This is corroborated through Figures 11–13, where the corrosion rate and cathodic kinetics decreased within increasing electrode spacing. Typically during processing, as the electrode size increases, the spacing also increases.[39]

Effect of AlO_2^- dissolution and redeposition on corrosion rate.—The dramatic increase in the measured cathodic current density with increasing area fraction is larger than a linear multiplication factor with respect to the Al area (Figures 5–7). It is proposed that the increase in the Al electrode area enhances cathodic activity due to both transition metal enrichment from impurities and Al cathodic corrosion and redistribution on the sample surface. At intermediate pH, the dominant reaction is the formation of Al oxide in the solid state:[55]

$$Al + 3H_2O \rightarrow Al_2O_3\,(s) + 6H^+ + 6e^- \qquad [4]$$

However, local alkalization of the surface occurs at the Mg/Al interface to pH∼11 (as shown in Figures 14b–14c), resulting in:

$$Al + 2H_2O \rightarrow AlO_2^- + 4H^+ + 3e^- \qquad [5]$$

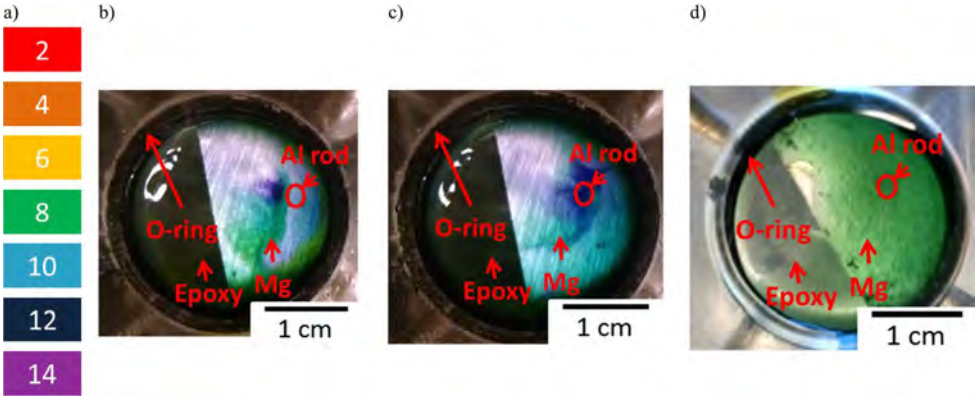

Figure 14. a) Key for pH colors as detected by universal pH indicator. Variation in the pH distribution with exposure environment for b) 0.6 M NaCl (starting pH∼5.3) immediately after adding the pH indicator, c) 5 minutes after adding the pH indicator and d) pH distribution in 0.1 M TRIS (starting pH∼7).

The Nernst potentials for each of these reactions at pH = 11 are −2.44 V_{SCE} and −2.50 V_{SCE} (assuming an AlO_2^- concentration of 10^{-6} M) which is much lower than the OCP of pure Mg (−1.63 V_{SCE}). According to the Al Pourbaix diagram[55] and knowledge of the thermodynamics of the system that Equation 4 is the dominant reaction when in near neutral solutions while Equation 5 is dominant in strongly alkaline (pH ≥ 11) solutions. The redistribution of the Al to the surrounding oxide is seen through EDS (Figure 15). The movement of the AlO_2^- away from the electrode creates a composition gradient which will increase the corrosion rate as the AlO_2^- spreads. This spreading is caused by the convection from the HER reaction, as well as the variation in the pH at the Mg/Al electrode interface in comparison to above the Mg.

The concentration gradient, C(r), of the AlO_2^- by diffusion released in solution from the IMP can be plotted assuming a one-dimensional radial diffusion from a spherical electrode according to:

$$\frac{C(r)}{C_{IMP}} = \frac{d}{r}\left[\text{erfc}\left(\frac{r-d}{2\sqrt{Dt}}\right)\right] \quad [6]$$

Where C_{IMP} is the concentration of dissolved AlO_2^- at the electrode (assumed to be 1 M), d is the diameter of the electrode, r is the radial distance away from the electrode, D is the diffusion coefficient of AlO_2^- in H_2O 1.0×10^{-9} m^2/s, erfc is the complementary error function and t is the time. For r ≥ d a concentration gradient is shown for the assumptions that $C(r)/C_{IMP} < 1$ and for r < d $C(r)/C_{IMP} = 1$. The concentration gradient, in the case of quiescent solution, after 3 and 24 hours in shown in Figure 18. Additional AlO_2^- transport by convection due to H_2 gas evolution at the Al/Mg interface has been excluded for this analysis. The radial distance outward was normalized (r/d); therefore, all the concentration gradients overlay one another. The concentration gradient approaches 0 at r/d = 10, therefore the electrodes can transport AlO_2^- over a radial distance approximately 10 times as large as their diameter in quiescent solution due to vigorous HER.

This zone functions as the location for cathodic activation in Mg alloys and corrosion initiation due to the Al redistribution as well as transition metal enrichment.[28,29] In a unbuffered chloride environment, the alkaline shift at these electrodes can lead to higher rates of AlO_2^- dissolution and possible Al redeposition away from the electrode. The effect of pH in the chloride-containing environment was measured using a universal pH indicator (Figure 14) in 0.6 M NaCl, where a large alkaline shift at the Al electrode was observed, which could lead to AlO_2^- release according to the half-cell reaction in Equation 5. Spreading of this pH indicator, likely due to stirring from the HER, can encourage redistribution of the Al along the surface. According to the Al Pourbaix diagram, at a pH above ∼9 the Al will begin to corrode according to Equation 5. This is reflected in Figure 3 where an area around the Al particle has corroded due to this higher pH gradient. Areas around the particle which have not corroded would similarly have not seen a pH above ∼9 and were less affected by the corrosion process.

However, in the chloride-free buffered environment, 0.1 M TRIS, little variation in the cathodic kinetics were seen for variations in the electrode area fraction, size or spacing (Figures 7, 10 and 13). It has been previously illustrated that little to no cathodic activation upon anodic polarization occurs in this environment.[10] At a buffered pH of ∼7–8 in this solution there is a lack of the thermodynamic possibility of $Al \rightarrow AlO_2^-$, as the dominant half-cell reaction produces Al_2O_3. However, Al will still act as a microcathode on the sample surface where the HER can readily occur. At a pH of ∼7 in the buffer, neither the Al or the Mg passivates. Instead, the dominant reaction is the dissolution of Mg (for all samples) and this is seen to control the corrosion rate. This is characterized by the equivalent cathodic reaction rates for all Al-containing samples at the same Al area ratio in the 0.1 M TRIS solution (Figures 7, 10 and 13). It is interpreted that corrosion is already very fast on the Mg surface, given the lack of oxide and the HER rate is high on bare Mg (Figure 6a). A secondary effect is the lack of an $Mg(OH)_2$ film in TRIS which leads to a faster corrosion rate and little to no metal enrichment within this hydroxide

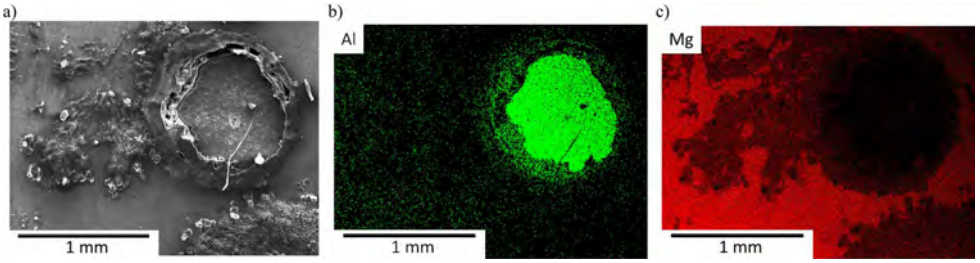

Figure 15. a) Corrosion product around Al electrode embedded in Mg, b) Al distribution after corrosion and c) Mg EDS after corrosion in 0.6 M NaCl.

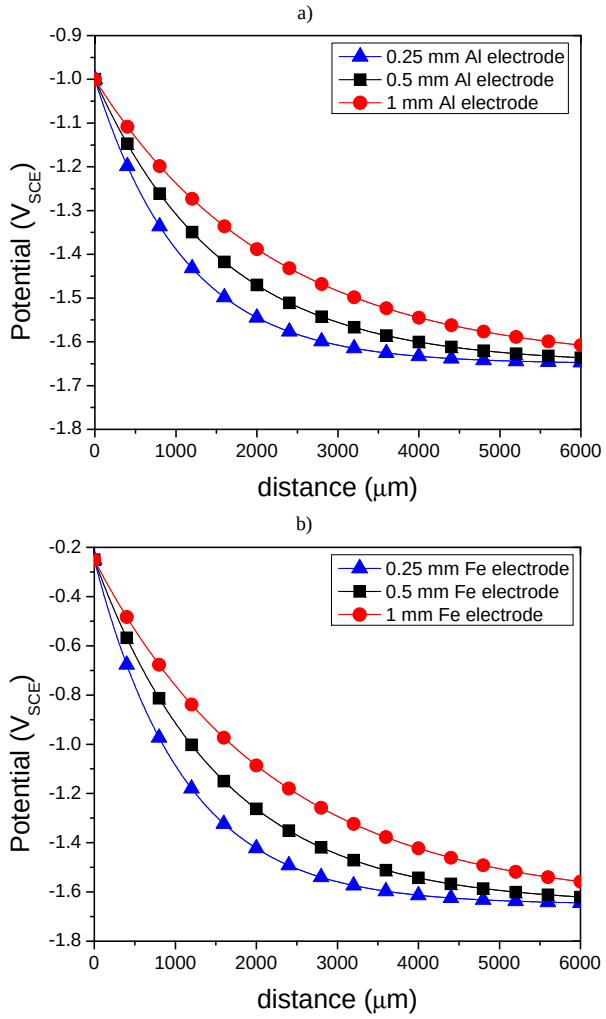

Figure 16. Effect of electrode size on potential distribution E(r) where $d = 0.25$ mm to $d = 1$ mm. As the electrode size increases, the throwing power increases for b) Al electrodes and b) Fe electrodes. $R_p = 90.8$ Ω-cm^2,[45], $p = 25\ \Omega^{-1}\text{cm}^{-1}$.

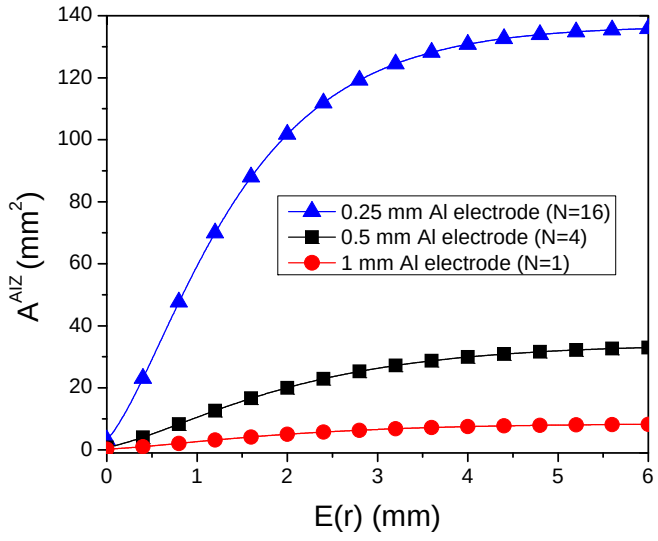

Figure 17. Area of anodically induced zone (A^{AlZ}) for a given potential distribution E(r) for different electrode sizes where the zone formed is due to Al redeposition[30,36] and transition metal enrichment[28,29] around the Al-rich electrodes. All samples retained the same area fraction of Al electrodes on the sample surface.

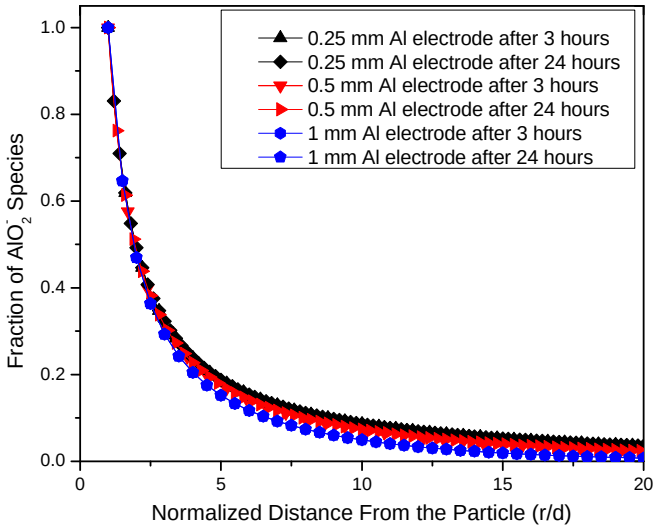

Figure 18. Variation in the radial concentration gradient of AlO_2^- away from the Al-rich IMP interface assuming a spherical particle for both Al-Mn and Al-Mn-Fe IMPS.

film can occur.[10] This could also lead to less cathodic activation with time.[26,28,32]

Conclusions

1. For the Mg-Al model alloys studied, the cathodic kinetics and open circuit corrosion rate were shown to increase with increasing area fraction of Al electrodes; as determined from EIS as well as DC cathodic polarization curves. The increase in cathodic kinetics provides a rationalization as to the mechanistic origin of increased corrosion rate; however it merits comment that the increase in the corrosion rate determined through the EIS method, was smaller than seen during cathodic polarization.
2. For a fixed area fraction of Al electrodes embedded in Mg, the cathodic kinetics and corrosion rate decrease with larger electrodes and increasing electrode spacing - due to less overlap of both galvanic potential and AlO_2^- chemical concentration fields in 0.6 M NaCl.
3. In the case of decreasing the Al electrode size, whilst maintaining the same total area fraction of Al, it was found that overall cathodic kinetics and corrosion rate increased indicated by significant increases in i_c ($-1.8\ V_{SCE}$) as well as $1/R_p$. This was an important finding, as it can be rationalized that with smaller electrode sizes yet the same area fraction, more fast cathodic sites exist in the array and therefore more sites for cathodic activation develop at the electrode/Mg interface and in the zones of cathodic activation created around Al-rich IMPs. This accounts for enhance corrosion kinetics and cathodic HER kinetics in the case of small, closely spaced Al electrodes in a Mg matrix. This conclusion is supported by a closely related study involving Al-rich IMPs whose size was varied by heat-treatment.[39]

Acknowledgments

This work was funded by the Office of Naval Research grant N000141210967 with Dr. David A. Shifler as scientific officer. The U.S. Government is authorized to reproduce and distribute reprints for Governmental purposes notwithstanding any copyright notation thereon. The views and conclusions contained herein are those of the authors and should not be interpreted as necessarily representing the Office of Naval Research and the Technical Corrosion Collaboration.

References

1. E. Ghali, in *Uhlig's corrosion handbook*, 2 ed., p. 793, John Wiley & Sons, new york (200).
2. T. B. Abbott, *Corrosion*, **71**, 120 (2015).
3. S. R. Agnew and J. F. Nie, *Scripta Mater*, **63**, 671 (2010).
4. T. Cain, L. Bland, N. Birbilis, and J. Scully, *Corrosion*, **70**, 1043 (2014).
5. D. A. Jones, *Prentice Hall* Upper Saddle River. NJ. (1996).
6. K. Gusieva, C. H. J. Davies, J. R. Scully, and N. Birbilis, *International Materials Reviews*, 169 (2014).
7. S. Lun Sin, D. Dubé, and R. Tremblay, *Materials Characterization*, **58**, 989 (2007).
8. O. Lunder, J. H. Nordlien, and K. Nisangliou, *Corrosion Reviews*, **15**, 439 (1997).
9. L. G. Bland, J. M. Fitz-Gerald, and J. R. Scully, *Corrosion*, **72**(9), 1116 (2016).
10. L. G. Bland, B. C. R. Troconis, R. J. Santucci, J. M. Fitz-Gerald, and J. R. Scully, *Corrosion*, **72**(10), 1226 (2016).
11. J. R. Kish, G. Williams, J. R. McDermid, J. M. Thuss, and C. F. Glover, *Journal of the Electrochemical Society*, **161**, C405 (2014).
12. G. L. Makar and J. Kruger, *Journal of the Electrochemical Society*, **137**, 414 (1990).
13. G. Song, L. M. Liu, M. S. Chi, and J. F. Wang, *Mater Sci Forum*, **488-489**, 371 (2005).
14. R. C. Zeng, J. Chen, W. Dietzel, R. Zettler, J. F. dos Santos, M. L. Nascimento, and K. U. Kainer, *Corros Sci*, **51**, 1738 (2009).
15. T. Zhu, Z. W. Chen, and W. Gao, *Materials Characterization*, **59**, 1550 (2008).
16. A. D. Südholz, N. T. Kirkland, R. G. Buchheit, and N. Birbilis, *Electrochemical and Solid-State Letters*, **14**, C5 (2011).
17. A. A. G. Song, *Advanced Engineering Materials*, **5**, 837 (2003).
18. G. S. Frankel, A. Samaniego, and N. Birbilis, *Corros Sci*, **70**, 104 (2013).
19. N. Birbilis, A. D. King, S. Thomas, G. S. Frankel, and J. R. Scully, *Electrochimica Acta*, **132**, 277 (2014).
20. G. S. Frankel, A. Samaniego, and N. Birbilis, *Corros Sci*, **70**, 104 (2013).
21. G. S. Frankel, S. Fajardo, and B. M. Lyncha, *faraday discussions*, **180**, 11 (2015).
22. G. Williams, H. ap Llwyd Dafydd, and R. Grace, *Electrochimica Acta*, **109**, 489 (2013).
23. G. Williams, N. Birbilis, and H. N. McMurray, *Electrochemistry Communications*, **36**, 1 (2013).
24. G. Williams, K. Gusieva, and N. Birbilis, *Corrosion*, **68**, 489 (2012).
25. G. Williams and H. N. McMurray, *Journal of the Electrochemical Society*, **155**, C340 (2008).
26. M. Taheri, J. R. Kish, N. Birbilis, M. Danaie, E. A. McNally, and J. R. McDermid, *Electrochimica Acta*, **116**, 396 (2014).
27. J. Swiatowska, P. Volovitch, and K. Ogle, *Corros Sci*, **52**, 2372 (2010).
28. T. Cain, S. B. Madden, N. Birbilis, and J. R. Scully, *Journal of the Electrochemical Society*, **162**, C228 (2015).
29. S. Fajardo and G. S. Frankel, *Electrochimica Acta*, **165**, 255 (2015).
30. M. Danaie, R. M. Asmussen, P. Jakupi, D. W. Shoesmith, and G. A. Botton, *Corros Sci*, **83**, 299 (2014).
31. M. P. Brady, G. Rother, L. M. Anovitz, K. C. Littrell, K. A. Unocic, H. H. Elsentriecy, G.-L. Song, J. K. Thomson, N. C. Gallego, and B. Davis, *Journal of the Electrochemical Society*, **162**, C140 (2015).
32. Z. P. Cano, M. Danaie, J. R. Kish, J. R. McDermid, G. A. Botton, and G. Williams, *Corrosion*, **71**, 146 (2015).
33. Z. P. Cano, J. R. McDermid, and J. R. Kish, *Journal of the Electrochemical Society*, **162**, C732 (2015).
34. M. Curioni, F. Scenini, T. Monetta, and F. Bellucci, *Electrochimica Acta*, **166**, 372 (2015).
35. M. Mokaddem, P. Volovitch, F. Rechou, R. Oltra, and K. Ogle, *Electochimica Acta*, **55**, 3779 (2010).
36. R. M. Asmussen, W. J. Binns, R. Partoci-Nia, P. Jakupi, and D. W. Shoesmith, *Materials and Corrosion*, **67**, 39 (2016).
37. R. C. Phillips and J. R. Kish, *Corrosion*, **69**, 813 (2013).
38. C. Xu, R. Wang, Y. Zhang, and Y. Ding, *Nanoscale*, **2**, 906 (2010).
39. L. G. Bland, J. J. Bhattacharyya, S. R. Agnew, J. M. Fitz-Gerald, and J. R. Scully, *Acta Materialia*, In Review (2016).
40. M. Esmaily, D. B. Blücher, J. E. Svensson, M. Halvarsson, and L. G. Johansson, *Scripta Mater*, **115**, 91 (2016).
41. M. K. Cavanaugh, N. Birbilis, R. G. Buchheit, and F. Bovard, *Scripta Mater*, **56**, 995 (2007).
42. G. Song and A. Atrens, *Adv Eng Mater*, **5**, 837 (2003).
43. L. G. Bland, A. D. King, N. Birbilis, and J. R. Scully, *Corrosion Journal*, **71**, 128 (2015).
44. *Oxford Instruments* (2015).
45. C. A. Schneider, W. S. Rasband, and K. W. Eliceiri, *Nature Methods*, **9**, 671 (2012).
46. ASTM-G1, *ASTM International*, G1 (2011).
47. D. Surf, Mountains Surface Imaging and Metrology Software, in.
48. A. D. King, N. Birbilis, and J. R. Scully, *Electrochimica Acta*, **121**, 394 (2014).
49. R. Baboian, *ASTM STP*, **576**, 5 (1976).
50. ASTM-81, *ASTM International*, G71 (2014).
51. J. R. Scully and D. E. Peebles, *MRS Online Proceeding Library* (1990).
52. R. G. Buchheit, Local corrosion of Al-Li-Cu alloys, in *Materials Science and Engineering*, University of Virginia, Charlotteville, VA (1991).
53. S. Jain, J. L. Hudson, and J. R. Scully, *Electrochimica Acta*, **108**, 253 (2013).
54. D. R. Banjade, S. D. Porter, B. M. McMullan, and J. N. Harb, *Journal of the Electrochemical Society*, **163**, C116 (2016).
55. M. Pourbaix, *Atlas of electrochemical equilibria in aqueous solutions*, National Association of Corrosion Engineers, Huston, TX (1974).

Journal of The Electrochemical Society, **164** (2) X1-X1 (2017)
0013-4651/2017/164(2)/X1/1/$33.00 © The Electrochemical Society

Erratum: Exploring the Effects of Intermetallic Particle Size and Spacing on the Corrosion of Mg-Al Alloys Using Model Electrodes [*J. Electrochem. Soc.*, 163, C895 (2016)]

L. G. Bland,[a] N. Birbilis,[a,b] and J. R. Scully[a]

[a]*Department of Materials Science and Engineering, University of Virginia, Charlottesville, Virginia 22904, USA*
[b]*Department of Materials Science and Engineering, Monash University, Victoria 3800, Australia*

The fourth sentence in the caption for Figure 9, on page C901, should read:

"a) Typical cathodic polarization curves for 3 mm spacing, b) 3 mm spacing, and c) 7 mm spacing."

The fourth sentence in the caption for Figure 10, on page C901, should read:

"a) Typical cathodic polarization curves for 3 mm spacing, b) 3 mm spacing, and c) 7 mm spacing."

The third sentence in the caption for Figure 12, on page C902, should read:

"Typical cathodic polarization curves for a) 0.5 mm diameter."

The second sentence in the paragraph directly below Eq. 3 on page C903 should read:

"With the same area fraction (but different numbers of electrodes, N), there is a decrease in the E(r) distribution via Eq. 2 on the smale surface for a smaller electrode size, as determined for 0.25 mm, 0.5 mm, and 1 mm diameter electrodes (Fig 16).

Figure 17 on page C905 is replaced with:

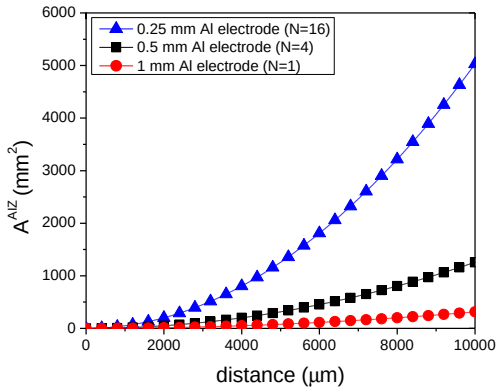

The Acknowledgments section should read:

"This work was funded by the Office of Naval Research grant N000141210967 and Grant SP0028970-PROJ0007990 with Dr. David A. Shifler as science officer and with additional support for John R. Scully supported by NSF DMR 130999. The U.S. Government is authorized to reproduce and distribute reprints for government purposes notwithstanding any copyright notation thereon. The views and conclusions contained herein are those of the authors and should not be interpreted as necessarily representing the Office of Naval Research."